ACS OMEGA

http://pubs.acs.org/journal/acsodf

Article

Hierarchical N-Doped CuO/Cu Composites Derived from Dual-Ligand Metal–Organic Frameworks as Cost-Effective Catalysts for Low-Temperature CO Oxidation

Jingwen Mao, Lei Qin, Lin Tian, Lantian He, Yujie Zhu, Qin Meng, and Guoliang Zhang*

Cite This: *ACS Omega* 2021, 6, 29596–29608

Read Online

ACCESS | Metrics & More | Article Recommendations | Supporting Information

ABSTRACT: Development of multi-ligand metal–organic frameworks (MOFs) and derived heteroatom-doped composites as efficient non-noble metal-based catalysts is highly desirable. However, rational design of these materials with controllable composition and structure remains a challenge. In this study, novel hierarchical N-doped CuO/Cu composites were synthesized by assembling dual-ligand MOFs via a solvent-induced coordination modulation/low-temperature pyrolysis method. Different from a homogeneous system, our heterogeneous nucleation strategy provided more flexible and cost-effective MOF production and offered efficient direction/shape-controlled synthesis, resulting in a faster reaction and more complete conversion. After pyrolysis, they further transformed to a unique metal/carbon matrix with regular morphology and, as a hot template, guided the orderly generation of metal oxides, eliminating sintering and agglomeration of metal oxides and initiating a synergistic effect between the N-doped metal oxide/metal and carbon matrix. The prepared N-doped CuO/Cu catalysts held unique water resistance and superior catalytic activity (100% CO conversion at 140 °C).

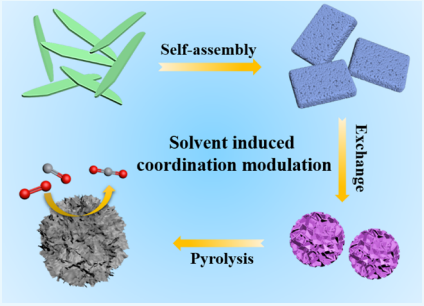

1. INTRODUCTION

Carbon monoxide (CO) oxidation is not only a model reaction commonly used in catalytic research but also an important process with practical significance.[1,2] Noble metal-based materials are excellent catalysts with very high performance for CO oxidation, but the difficult recovery and high cost prevent them from universal applications.[3,4] It is essential to improve the utilization rate of precious metals or develop other non-noble metal materials with high performance. In the field of noble metal catalysts, gold (Au) has a large amount of mining, a lower price, and a more mature recovery technology, which is suitable as a substitute for noble metals such as Pd and Pt.[5] Furthermore, Au-based catalysts show significant humidity enhancement in CO oxidation reactions, and single Au atoms, Au clusters (1–2 nm), and Au NPs (2–5 nm) dispersed on solid supports have caused extensive research because they can achieve high and stable catalytic efficiency with less precious metal loading.[6,7] Recently, the alternatives like non-noble metal-based catalysts, especially transition metal oxides (Co_3O_4, CuO, MnO_2, etc.), are attracting much interest due to the availability of raw materials, simple preparation, and low price.[8−10] However, the reaction performance of most non-noble metal catalysts is currently not comparable to that of noble metals, especially under a moisture-rich condition.[11−13] It is worth mentioning that the cerium oxide (CeO_2)-supported CuO or Cu catalyst has been considered as an economical and efficient material since the CeO_2 support can effectively activate oxygen to accelerate the rate of CO conversion. In addition, thermally or hydrothermally treated Cu/CeO_2 catalysts have been reported to exhibit excellent activity and stability for low-temperature CO oxidation.[14−16] Although there are some reports on improving copper-based catalysts by supporting or combining other metal materials, few studies are focused on the development of the structure of CuO itself, especially the exploration of novel CuO materials with multiple non-metallic components.

Metal–organic frameworks (MOFs) as a new class of organic–inorganic hybrid materials possess ultra-high specific surface areas, adjustable pore structures, and surface multifunctionalities.[17,18] These characteristics make MOFs promising templates for preparation of nanostructured metal oxides with complex compositions and diversified structures.[19,20] Since most MOFs take transition metals (Cu, Co, Ni, Fe, Mn, etc.) as the central metal, which are usually essential elements in CO oxidation, the derivatives with the same basic compositions as parent MOFs have great potential in CO oxidation.[21−24] In addition, due to the wide variety of MOFs and their diversified structures, a suitable MOF matrix can be transformed into porous specific functionalized composites

Received: July 21, 2021
Accepted: September 30, 2021
Published: October 25, 2021

such as heteroatom doping (N, S, P, etc.) or polymetallic (bimetallic, trimetallic, etc.) hybrid materials, which are significant for enhancing the activity of catalytic sites.[25−28] Therefore, the rational design on the structure and composition of MOF precursors is very essential for development of high-performance derivatives.

Over the past decades, most derived catalysts were obtained by pyrolysis of classical MOFs with a single structure. The lack of available heteroatom-rich MOFs as single-source precursors for carbonization seems to be a big deficiency in the progress of catalytic oxidation. To impart new functionalities and structures, the introduction of extra heteroatom-rich ligands into the MOF host (i.e., dual-ligand MOFs) has attracted attention recently.[29−31] So far, two main ways are explored to construct multi-ligand MOFs including modifying ligands before and after synthesis. The first strategy is carried out by mixing different ligands with soluble metal salts and then prepared by a hydrothermal method.[32,33] The second route is performed via ligand exchange after the synthesis of MOFs.[34,35] However, no matter how the one-pot hydrothermal method or post-synthetic modification method behaves, the formation of multi-ligand MOFs by ionic metal precursors in a homogeneous system often needs a high extra-energy consumption (≥80 °C) and long reaction time (between 1 and 2 days). Moreover, the introduction of a second ligand into the original MOFs may cause severe collapse of the intrinsic morphology. Comparatively, the heterogeneous nucleation strategy with insoluble metal precursors such as metal oxides and metal hydroxides would provide a more flexible and cost-effective route for MOF production and offer an efficient route for direction- and shape-controlled synthesis.[36−39] Superior to traditional methods, development of a heterogeneous assembly strategy exhibits greater potential to fabricate multi-ligand MOFs for rapid transformation of derivatives with complex compositions and unique structures.

In the present work, we proposed a facial approach to the design and synthesis of hierarchical N-doped CuO/Cu composites (N-CuO/Cu) derived from dual-ligand MOFs by a solvent-induced coordination modulation/low-temperature pyrolysis method (Scheme 1). Different from metal ions in a homogeneous system, insoluble metal complexes had higher lattice enthalpies and high-density nucleation sites, which generated strong directional binding energy between double ligands, resulting in a faster reaction time and more complete conversion. After pyrolysis, the insoluble metal complex further transformed into a unique metal/carbon matrix with regular morphology and, as a hot template, guided the orderly generation of metal oxides, thereby overcoming the difficulties of sintering and agglomeration of metal oxides caused by weak metal ion binding points and creating a synergistic catalytic surface between the oriented N-doped metal oxide/metal and carbon matrix. Our method has the following features: (1) the incorporation of a heteroatom-rich ligand into MOF channels and cavities can be used to adjust the surface and internal properties of derivatives easily and provide spatial and surface active sites for various catalysts; (2) formation of an MOF sol can effectively avoid coordination competition between double ligands, which should be more conducive to produce dual-ligand MOFs with high crystallinity and purity; and (3) multi-component hybrid materials can be synthesized by carbonizing dual-ligand MOFs without additional sources for efficient catalytic oxidation. This strategy is applicable for the rapid introduction of a broad range of heteroatom-rich ligands into metal-based MOFs and rapid transformation of derivatives with complex compositions and unique structures. The derived heteroatom-doped metal oxides showed excellent catalytic activity and maintained unique stability even under a water vapor atmosphere.

Scheme 1. Schematic Illustration of the Synthesis of CuBDC-MeIM(rt) Nanoflowers and the Derived N-CuO/Cu Catalysts

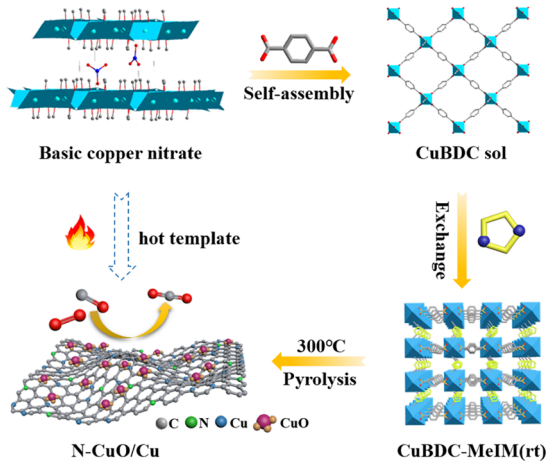

2. RESULTS AND DISCUSSION

2.1. Formation Mechanism of CuBDC-MeIM(Rt). In the beginning, insoluble basic copper nitrate and soluble copper nitrate were used as metal sources to compare and study the mechanism of the formation of dual-ligand MOFs (Figure 1). We first employed copper nitrate to react with DMF to generate insoluble basic copper nitrate (Figure 1c). Then, H_2BDC was added to the $Cu_2(OH)_3(NO_3)$ and $Cu(NO_3)_2\cdot 3H_2O$ solutions, and a blue sol was immediately formed in the $Cu_2(OH)_3(NO_3)$/BDC solution, but no substance was found in the $Cu(NO_3)_2\cdot 3H_2O$/BDC solution (Figure 1d). This is because DMF had stronger coordination ability with metal ions than methanol. After a period of reaction, DMF molecules and Cu^{2+} formed a copper-based complex with a regular morphology, and the complex was used as an insoluble copper-based precursor. The insoluble precursor was rapidly transformed in a solution containing H_2BDC to form a sol containing dispersed Cu-based metal organic nanoparticles.[40,41] Additionally, the Tyndall effect that was observed in the blue sol further indicated the formation of colloids (Figure S1). The XRD spectrum showed that the blue colloids belonged to CuBDC, confirming the coordination between $Cu_2(OH)_3(NO_3)$ and H_2BDC (Figure 2a,b). Obviously, the solvent-induced heterogeneous nucleation overcame the high energy barrier of homogeneous nucleation and accelerated the smooth transformation of the precursor into CuBDC.[42,43] After adding 2-MeIM to the CuBDC sol, the solution changed from blue to purple (Figure 1e). Comparing the XRD patterns of CuBDC-MeIM prepared by post-synthesis exchange and the one-pot method, it was verified that the purple product belonged to CuBDC-MeIM, proving that the dual-ligand MOF was successfully obtained by this method (Figure 2c). For 2-MeIM, the strength of the N-transition metal bond is greater than that of the O-transition metal bond, and the unshared electron pair of the N atom can easily compete with O

https://doi.org/10.1021/acsomega.1c03877
ACS Omega 2021, 6, 29596−29608

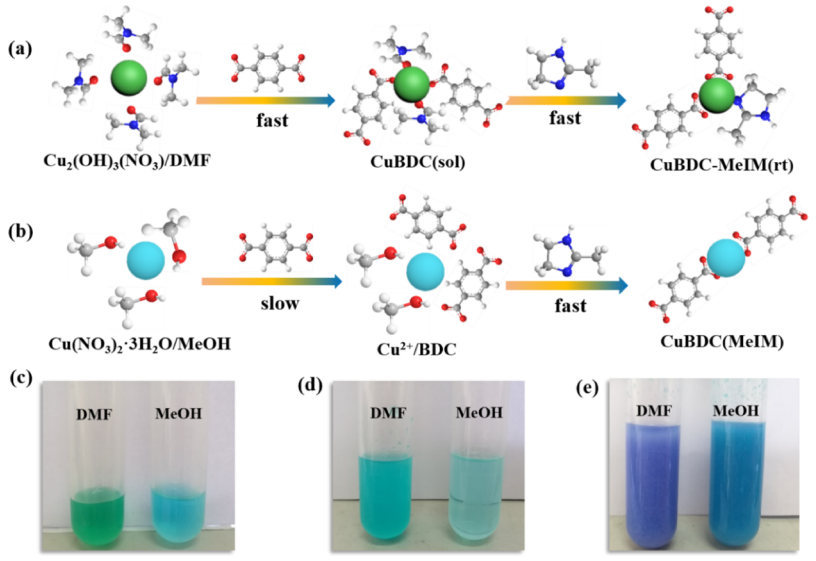

Figure 1. Kinetic step of (a) preparing CuBDC-MeIM(rt) with basic copper nitrate as a metal source and (b) preparing CuBDC(MeIM) with soluble copper nitrate as a metal source. (c) Phenomenon of $Cu_2(OH)_3(NO_3)$ and $Cu(NO_3)_2{\cdot}3H_2O$. (d) Phenomenon of the CuBDC sol and $Cu(NO_3)_2{\cdot}3H_2O/H_2BDC$ mixture. (e) Phenomenon of CuBDC-MeIM(rt) and CuBDC(MeIM).

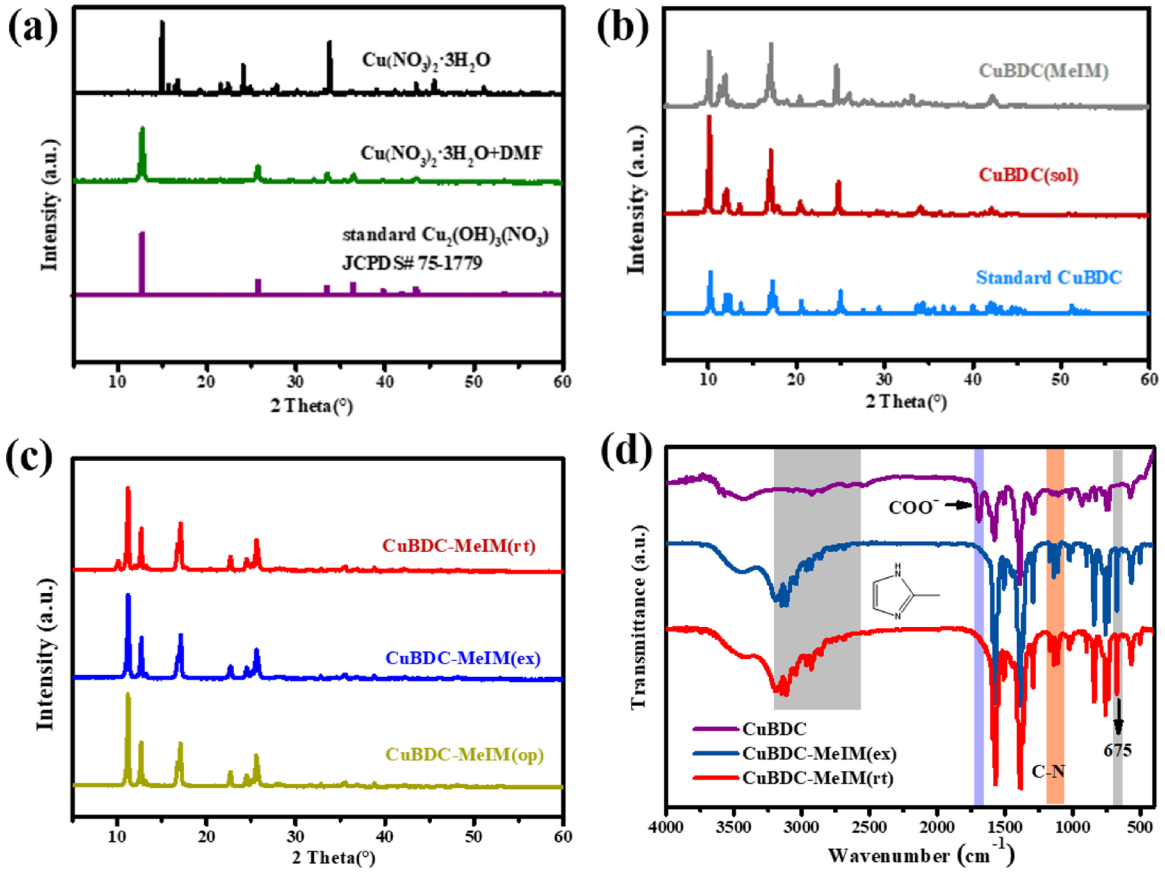

Figure 2. (a) Powder XRD patterns of $Cu(NO_3)_2{\cdot}3H_2O$, $Cu(NO_3)_2{\cdot}3H_2O{\cdot}$DMF, and standard $Cu_2(OH)_3(NO_3)$. (b) Powder XRD patterns of CuBDC(MeIM), CuBDC sol, and standard CuBDC. (c) Powder XRD patterns of CuBDC-MeIM(rt), CuBDC-MeIM(ex), and CuBDC-MeIM(op). (d) FTIR spectra of CuBDC, CuBDC-MeIM(ex), and CuBDC-MeIM(rt).

electrons on the ligand BDC or the O electrons at the uncoordinated Cu−O bond.[44] Therefore, in the $Cu_2(OH)_3(NO_3)$/BDC system, besides accelerating the deprotonation of the uncoordinated H_2BDC, 2-MeIM underwent a coordination or substitution reaction on the formation of the CuBDC framework, and the co-promotion of solvents and competing ligands enabled rapid nucleation of dual-ligand MOFs at room temperature. While in the $Cu(NO_3)_2{\cdot}3H_2O$/BDC system, 2-MeIM only acted as a competitive ligand to accelerate the deprotonation of H_2BDC and promote the

https://doi.org/10.1021/acsomega.1c03877
ACS Omega 2021, 6, 29596−29608

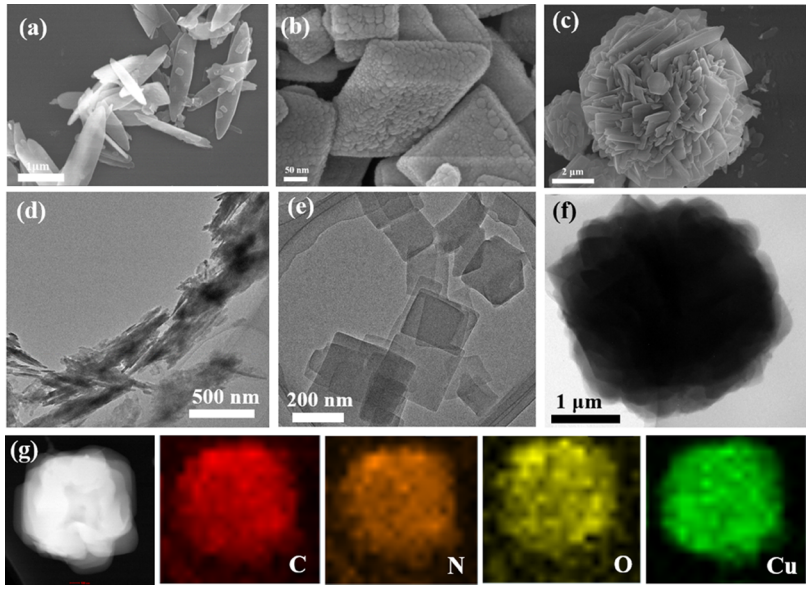

Figure 3. SEM and TEM images of (a, d) $Cu_2(OH)_3(NO_3)$ nanosheet, (b, e) CuBDC sol, and (c, f) flower-like CuBDC-MeIM(rt) and (g) EDX mappings of the different elements O, N, and Cu recorded from an individual CuBDC-MeIM(rt).

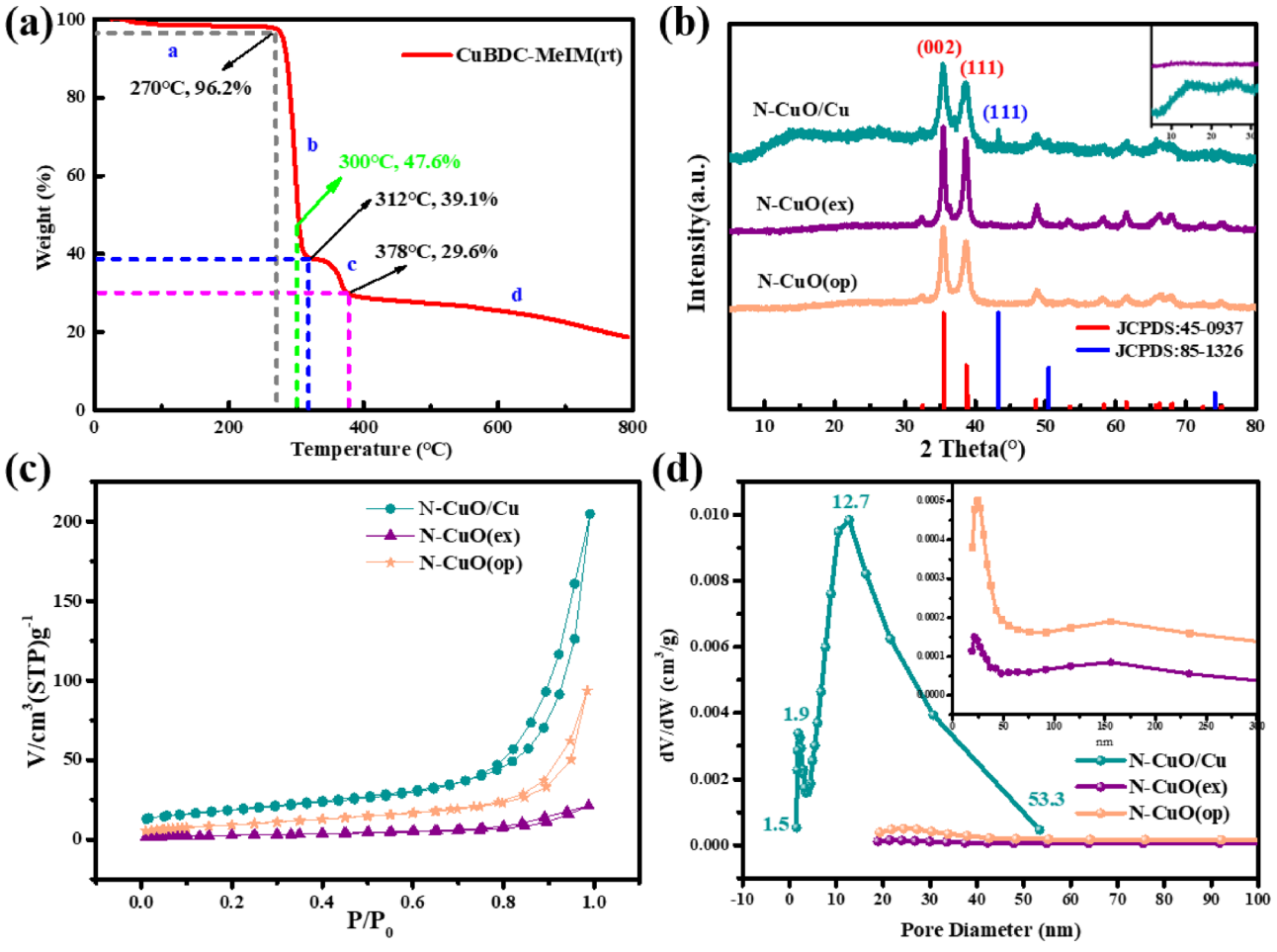

Figure 4. (a) TG curves of CuBDC-MeIM(rt). (b) XRD patterns of CuBDC-MeIM(rt), CuBDC-MeIM(ex), and CuBDC-MeIM(op) after pyrolysis at 300 °C. (c) Adsorption/desorption isotherms for N-CuO/Cu, N-CuO(ex), and N-CuO(op). (d) BJH patterns of N-CuO/Cu, N-CuO(ex), and N-CuO(op).

formation of CuBDC.[45] The generation of the CuBDC sol was the key to obtain dual-ligand MOFs. The reaction system of CuBDC sol and 2-MeIM was equivalent to the post-synthetic modification system. The difference was that CuBDC powder

https://doi.org/10.1021/acsomega.1c03877
ACS Omega 2021, 6, 29596−29608

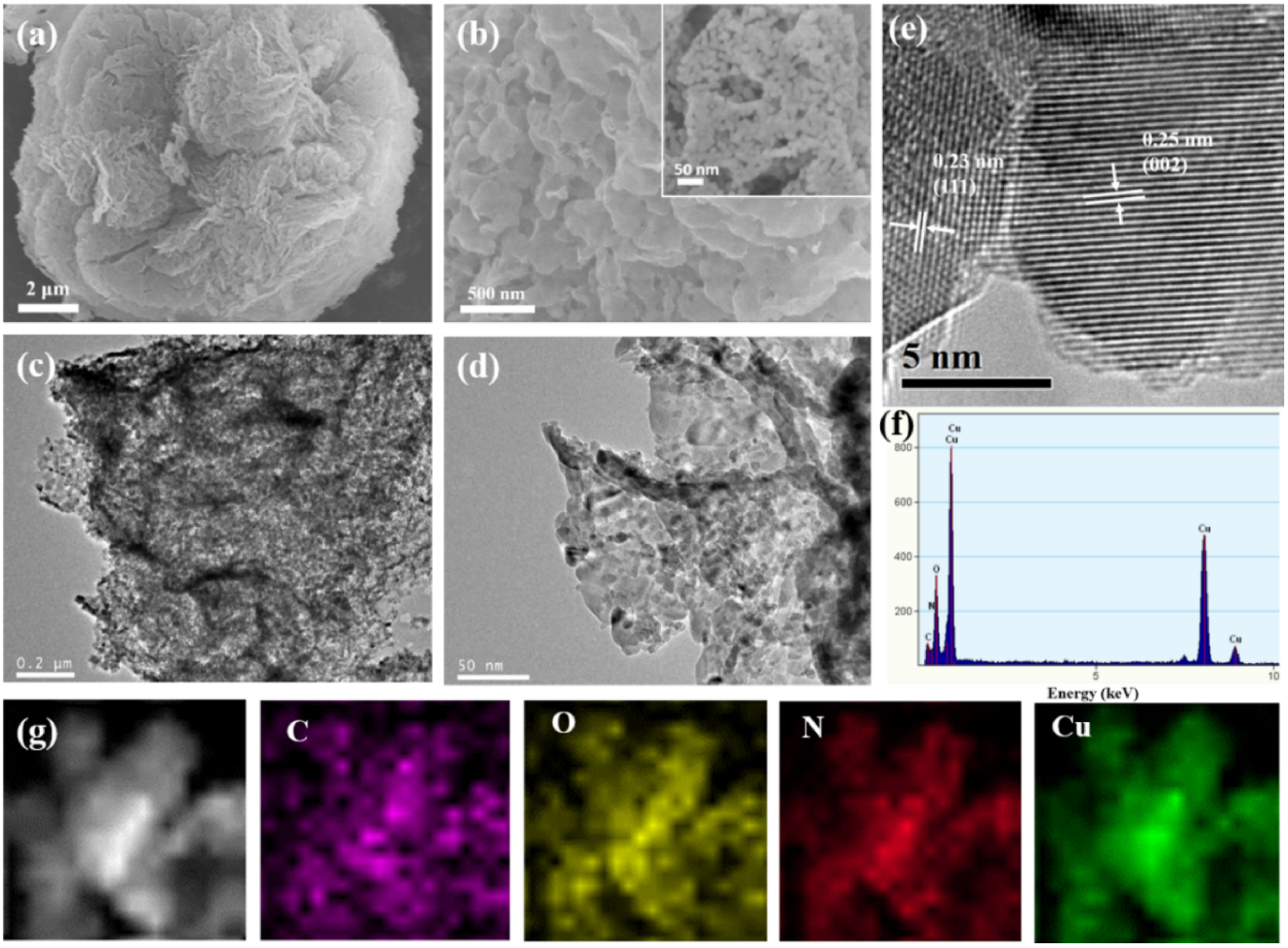

Figure 5. (a, b) SEM images of N-CuO/Cu. (c, d) TEM image of N-CuO/Cu. (e) Higher magnification and (f, g) EDX mappings of N-CuO/Cu.

did not need to be prepared in advance, and the processes of MOF synthesis and ligand exchange were performed almost simultaneously.[34] Comparisons on FTIR results of CuBDC, CuBDC-MeIM(ex), and CuBDC-MeIM(rt) (Figure 2d) clearly showed that the characteristic peak of −COOH at 1690 cm^{-1} was only observed on CuBDC.[46] The uncoordinated H_2BDC molecules remained in the framework of CuBDC, but the incorporation of 2-MeIM promoted the deprotonation of H_2BDC and coordination between Cu^{2+} and H_2BDC. In the CuBDC-MeIM spectrum, the small characteristic peaks appearing at 3200−2800 cm^{-1} corresponded to the $-CH_3$ and C−H vibrational peaks of 2-MeIM. The C−N peak at 1350−1000 cm^{-1} and C═C cis functional peak of the imidazole ring at 675 cm^{-1} well demonstrated that 2-MeIM was coordinated with CuBDC.[47]

SEM and TEM images were used to observe the morphological changes of the products. Basic copper nitrate displayed a fusiform structure (Figure 3a,d), which was used as the direction and shape guide agent in the formation of the CuBDC sol. The prepared CuBDC sol was composed of many particles with a particle size of about 10 nm (Figure 3b,e). Compared with CuBDC prepared by traditional methods (Figure S2), the obtained CuBDC sol had a more regular nanosheet structure and uniform size (200 nm × 50 nm). Subsequently, the introduction of 2-MeIM changed the original two-dimensional layered structure of CuBDC. Comparing the morphology of CuBDC-MeIM prepared by the post-synthesis exchange and one-pot method, introducing a second ligand, 2-MeIM, into the CuBDC sol precursor led to the self-assembly of a flower-like 3D superstructure interconnected by nanosheets with uniform size (Figure 3c,f). CuBDC-MeIM(ex) presented a chaotic and disordered nanosheet structure, without forming a regular shape, and the nanosheets were partially agglomerated (Figure S3a). CuBDC-MeIM(op) had a similar flower-like structure, but the morphology was imperfect and the size was uneven, and due to the hydrothermal condition, the obtained CuBDC-MeIM(op) had a certain degree of agglomeration (Figure S3b). In short, CuBDC-MeIM(rt) prepared by this method had the best morphology and structure. The surface elements of three dual-ligand MOF materials were analyzed by an XPS test (Figure S4). Different from the case of CuBDC, the introduction of 2-MeIM into all of three dual-ligand MOF materials successfully led to the production of heteroatomic nitrogen. Among them, the nitrogen content in CuBDC-MeIM(rt), CuBDC-MeIM-(ex), and CuBDC-MeIM(op) accounted for 14, 4.53, and 12.25%, respectively. Importantly, EDS elemental mapping of CuBDC-MeIM(rt) well displayed that Cu, N, and O elements were uniformly distributed within the porous composites (Figure 3g).

2.2. Characterization of N-CuO/Cu. TGA was further performed to determine the pyrolysis temperature of CuBDC-

https://doi.org/10.1021/acsomega.1c03877
ACS Omega 2021, 6, 29596−29608

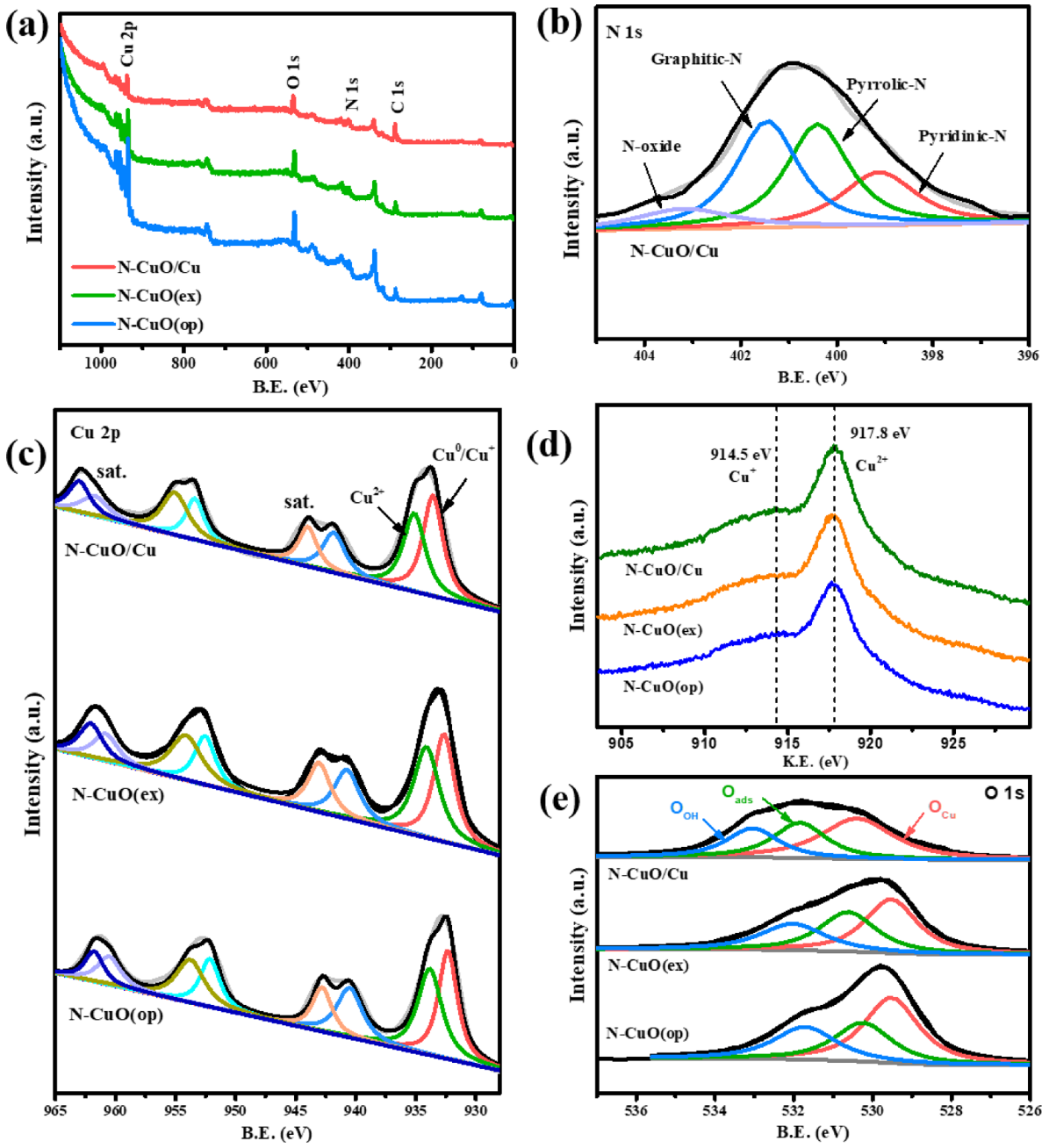

Figure 6. (a) Survey XPS spectra of N-CuO/Cu, N-CuO(ex), and N-CuO(op). (b) N 1s XPS spectra of N-CuO/Cu. (c) Cu 2p XPS spectra of N-CuO/Cu, N-CuO(ex), and N-CuO(op). (d) Kinetic energy spectra of the Auger L3VV electron of N-CuO/Cu, N-CuO(ex), and N-CuO(op). (e) O 1s XPS spectra of N-CuO/Cu, N-CuO(ex), and N-CuO(op).

MeIM(rt) (Figure 4a). The pyrolysis process can be divided into four stages. When the pyrolysis temperature was below 278 °C, the weight of the sample was almost unaffected by the increase in temperature, and a small amount of weight loss was attributed to moisture in the air bound to the sample.[28] The MOF framework rapidly decomposed at 278 °C and was completely converted to CuO at 313 °C. The organic ligands H_2BDC and 2-MeIM quickly decomposed into a carbon framework and doped N atoms. There was about 10% weight loss in the third stage, which may be attributed to the existence of hierarchical structures.[48] After raising the temperature to 800 °C, the residual amount of CuBDC-MeIM(rt) was 18.8 wt %, slightly higher than the copper content (13.72%). Based on the above TGA results, the samples were calcined at 300 °C in air to obtain the metal-based composites.

By comparing the XRD spectra of the products derived from the three dual-ligand MOFs, it was found that the main component of the derivative catalyst was CuO (Figure 4b). The difference was that in the N-CuO/Cu spectrum, the new diffraction peak appearing at 43.3° belonged to the simulated Cu(111) (JCPDS no. 85-1326). The apparent dispersion peaks on the left side (in the range 2θ = 10−30°) pointed to the amorphous carbon matrix,[49] indicating the formation of a Cu(111)/C matrix, and the final state of the derivative of CuBDC-MeIM(rt) was a N-doped CuO/Cu catalyst. The porous texture of N-CuO/Cu, N-CuO(ex), and N-CuO(op) were characterized by N_2 sorption at 77 K (Figure 4c). The

https://doi.org/10.1021/acsomega.1c03877
ACS Omega 2021, 6, 29596−29608

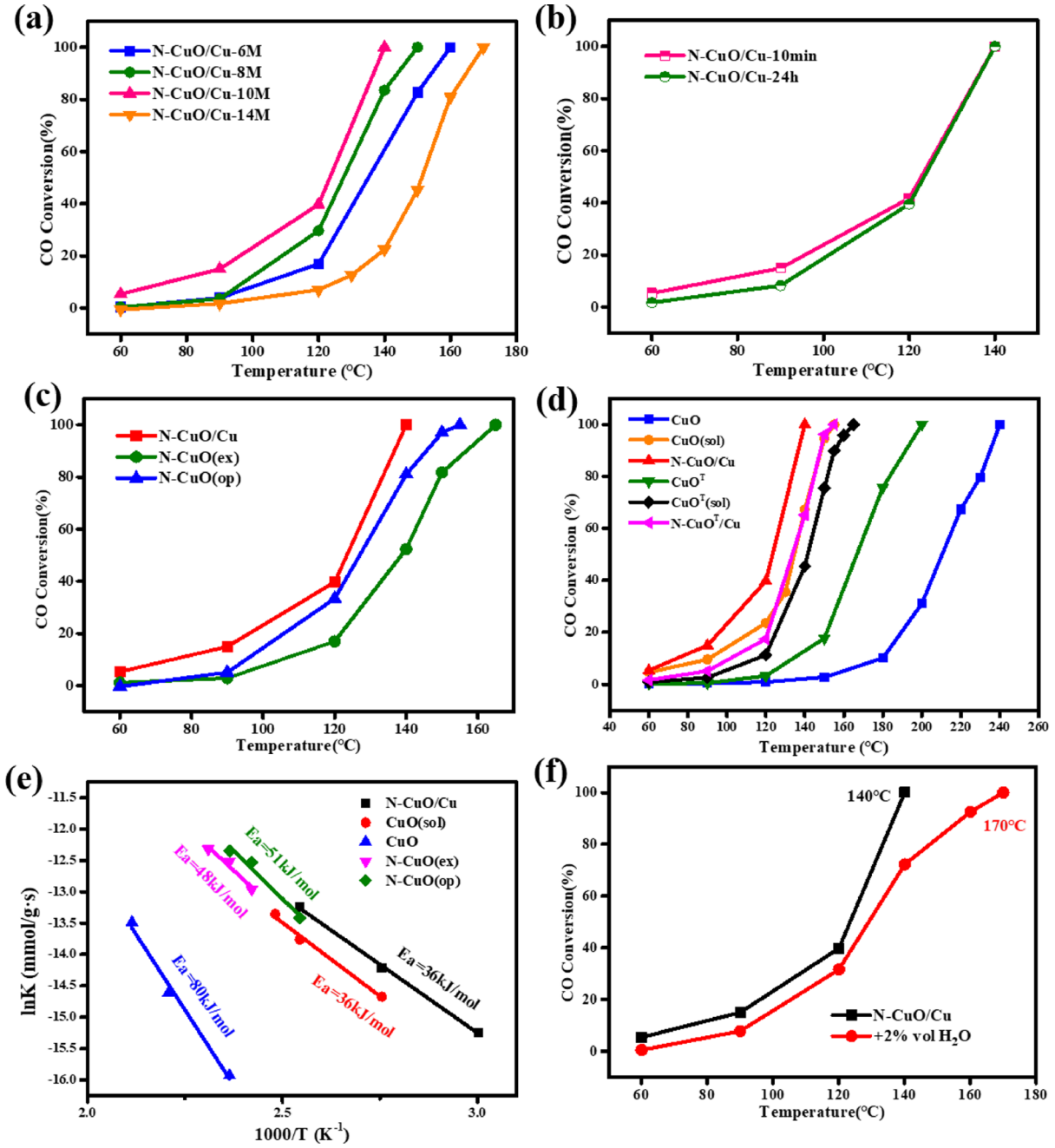

Figure 7. (a) CO conversion as a function of reaction temperature under different added 2-MeIM concentrations. (b) CO conversion as a function of reaction temperature under different synthesis reaction times. (c) CO conversion as a function of reaction temperature under different preparation methods. (d) Comparison of CO catalysis of MOF derivatives (traditional CuBDC/BTC, CuBDC/BTC sol, and CuBDC/BTC-MeIM). (e) Corresponding Arrhenius plots for the reaction kinetics. (f) Catalytic activities of N-CuO/Cu for CO oxidation under moisture-rich conditions (~2% H_2O).

isotherms of the three samples could be categorized as type IV with the H_3 hysteresis loop, in accordance with mesoporous materials.[25,27,28] As comparison, N-CuO/Cu exhibited higher Brunauer−Emmett−Teller surface areas (S_{BET}, 66.099 m^2/g) than samples N-CuO(ex) (9.882 m^2/g) and N-CuO(op) (34.421 m^2/g). The increase in S_{BET} can be attributed to the inherited hierarchical flower-like framework providing more complex spatial components for N-CuO/Cu.[50] Confirmed by the pore diameter distribution curves (Figure 4d), N-CuO/Cu exhibited rich micropores and mesopores and showed a distinct peak centered at 1.9 and 12.7 nm, whereas N-CuO(ex) and N-CuO(op) consisted of only mesopores and micropores. Furthermore, the total pore volume of N-CuO/Cu (0.316731 cm^3/g) was significantly larger than those of N-CuO(ex) (0.031763 cm^3/g) and N-CuO(op) (0.141293 cm^3/g). The large surface area, pore volume, and hierarchical pore structure were very beneficial to the exposure of active sites and rapid transportation of gas molecules to catalytic sites.[25,50]

As shown in the SEM images of the N-doped CuO/Cu sample, the self-assembly of nanoparticles was directed from CuBDC-MeIM(rt) to construct N-CuO/Cu hierarchical structures, which had an inherited flower-like structure consisting of nanosheets (Figure 5a−d). It was observed that the derivatives of CuBDC-MeIM(ex) and CuBDC-MeIM(op)

https://doi.org/10.1021/acsomega.1c03877
ACS Omega 2021, 6, 29596−29608

presented a sheet-like structure, with a size of approximately 100 μm × 5 μm (Figure S5), there was no obvious hierarchical structure, this was attributed to the fact that CuBDC-MeIM(rt) had the complete and well-shaped flower-like structure, and using fusiform basic copper nitrate as the metal node, the strong bond between the metal and the ligand prevented the collapse of the structure after pyrolysis.[51] The morphological properties of CuBDC-MeIM(rt) pyrolyzed at 573 K significantly affected the physicochemical properties of MOF-derived composites. Through the heat treatment, CuBDC-MeIM(rt) were converted to CuO/amorphous carbon with clear lattice fringes of 0.23 and 0.25 nm corresponding to the (111) and (002) crystal facets of CuO (JCPDS no. 45−0937) (Figure 5e), respectively. Importantly, EDS mappings of N-CuO/Cu well displayed that Cu, N, and O active sites were uniformly distributed within composites (Figure 5f,g).

More details on the chemical structure and surface oxidation state of N-doped CuO/Cu were carried out by XPS measurement. The presence of N was clearly observed in the XPS survey spectra of the three samples (Figure 6a). The fine N 1s survey spectra were deconvoluted into four peaks centered at 399.1, 400.4, 401.4, and 403.2 eV, corresponding to pyridinic-N, pyrrolic-N, graphitic-N, and N-oxide, respectively (Figure 6b).[25] The existence of pyridinic-N, pyrrolic-N, and graphitic-N indicates the successful doping of N atoms into the carbon layers. Benefiting from the doping of N atoms into the carbon layers, the CO catalytic performance of CuO could be further improved.[52] In order to further verify the effective doping of N element in three samples, the organic element analysis test (CHNS) was carried out. The results showed that the samples contained a certain amount of N element, and N-CuO/Cu contained the most N element, the doping amount was 2.5 wt %, while N-CuO(ex) and N-CuO(op) only contained 0.56 and 1.3 wt % of N element content. The results show that by using CuBDC-MeIM(rt) as the sacrificial template, more N-doped derivative catalysts can be obtained. For all three samples, the Cu 2p spectra can be divided into four peaks (Figure 6c). The main peak around 935 eV was assigned to lattice Cu^{2+} cations, and the presence of shake-up satellite peaks at 941 eV confirmed the existence of Cu^{2+}. As the binding energy of Cu^{2+} ranges from 934 to 935 eV, the lower binding energy suggested the presence of Cu^{+} or Cu^{0}.[49] In general, the relative intensity of the satellite relative to the main line in the standard Cu 2p spectrum was 0.55, and it was found that the relative intensities of N-CuO/Cu, N-CuO(ex), and N-CuO(op) were 0.43, 0.51, and 0.51, respectively.[14] The results indicated that N-CuO/Cu contained more Cu^{+} species. Generally, the Cu 2p spectra cannot be used to distinguish Cu^{0} and Cu^{+} species as they are essentially identical. However, their Auger parameters were different. Figure 6d shows the Cu L3VV spectrum of the three catalysts. The double peaks in the Cu L3VV spectra indicated the presence of two Cu species. The main peak in KE = 917.8 was assigned to Cu^{2+}. However, the shape of the peak was not symmetrical. A broadening toward lower energies was observed in all samples, indicating the presence of Cu^{+}.[9] The existence of Cu^{+} species may be the result of the strong interaction between copper species and porous carbon caused by nitrogen doping. Generally, in metal oxides, Cu^{+} had better CO catalytic activity than Cu^{2+}, and the activity of the catalysts was evaluated by the fraction of Cu^{+} ($Cu^{+}/(Cu^{+} + Cu^{2+})$). The larger the fraction of Cu^{+}, the better the catalytic effect was.[53] The ratio of Cu^{+} was calculated from the ratio of the area of the Cu^{+} peak to the main Cu $2p_{3/2}$ peak, the fractions of Cu^{+} ($Cu^{+}/(Cu^{+} + Cu^{2+})$) in the three catalysts were 0.54, 0.49, and 0.49, respectively, indicating that N-doped CuO/Cu had a better CO catalytic effect. Oxygen properties were analyzed in detail through the O 1s spectra. As displayed in Figure 6e, the spectra of O 1s for three samples were resolved into three peaks and contributed to O_{Cu} (lattice oxygen), O_{ads} (surface oxygen), and O_{OH} (absorbed water).[10,54] Furthermore, in situ DRIFTS measurement (Figure S6) was carried out to prove the composition of oxygen-containing substances on the surface. From the area percentages of different O elements calculated from XPS spectra, N-CuO/Cu contained the largest amount of lattice oxygen and lowest absorbed water species of all, which significantly improved the surface redox reaction, thus enhancing the catalytic performance and surface water resistance.

2.3. Catalytic Performance of CO Oxidation. The catalytic oxidation of CO was used as a model reaction. As depicted in Figure 7a, by adjusting the concentration of added 2-MeIM, a series of derived catalysts were obtained. ICP analysis showed that with the addition of 10 mmol of 2-MeIM, the MOF precursors contained the highest Cu content, indicating that under the operating conditions, Cu^{2+} achieved the maximum coordination. The CO catalytic test verified that N-CuO/Cu-10M exhibited superior catalytic performance with 100% CO conversion at 140 °C. The effects of reaction time on the catalytic performance of the derivatives were tested. As shown in Figure 7b, there was no difference in the catalytic effects of the catalysts obtained by reacting for 10 min and 24 h, both of which completely oxidized CO at 140 °C, indicating that 2-MeIM was completely coordinated in a short time. Furthermore, compared with N-CuO(ex) and N-CuO(op), N-CuO/Cu showed the best catalytic effect (Figure 7c). This is mainly due to the fact that N-CuO/Cu had the highest N doping content and higher lattice oxygen, providing more catalytically active sites. It was confirmed from Table S1 that the N-CuO/Cu catalyst had the highest Cu species dispersion (14.57%) and the highest active area (98.56 m^2/g). The order of the degree of dispersion of Cu species in different catalysts was as follows: CuO < N-CuO(ex) < N-CuO(op) < N-CuO/Cu, indicating that N doping led to better CuO dispersion. From the activity test results of the catalysts, we found that this sequence was almost the same as the selective sequence for the complete conversion of CO to CO_2, confirming the enhancement of catalytic activity caused by N doping. On the other hand, the Cu(111) crystal plane appearing in the N-CuO/Cu composite material was more conducive to the interaction between CuO and O_2 and greatly promoted the CO catalytic reaction.[55,56] In order to better clarify the superiority of using insoluble metal complexes as metal nodes, the catalytic performance of CuO derived from CuBDC and CuO(sol) derived from CuBDC sol was compared. As shown in Figure 7d, CuO exhibited the lowest catalytic performance for CO oxidation (total conversion at 240 °C), while CuO(sol) can completely oxidize CO at 155 °C. Based on the dispersion of Cu species and the content of CuO, the turnover frequency (TOF) values of CuO and N-CuO/Cu were calculated. N-CuO/Cu composites possessed a competitively high TOF value of 1.17×10^{-3} s^{-1} at 393 K, which was 1−2 orders of magnitude higher than CuO (6.99×10^{-5} s^{-1}) and superior to most reported MOF-based catalysts (Table S2). In sharp contrast, the lowest apparent activation energy (36 kJ/mol)

https://doi.org/10.1021/acsomega.1c03877
ACS Omega 2021, 6, 29596−29608

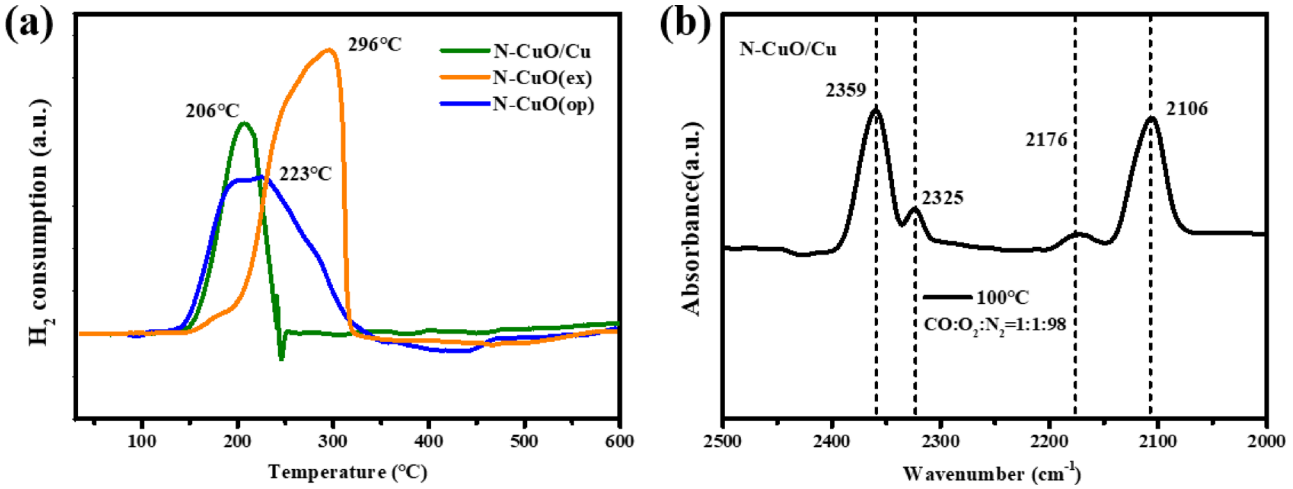

Figure 8. (a) H_2-TPR profiles of N-CuO/Cu, N-CuO(ex), and N-CuO(op) catalysts. (b) In situ DRIFT spectra of N-CuO/Cu after exposure to CO + O_2 at 100 °C for 10 min.

toward CO oxidation was observed for N-CuO/Cu (Figure 7e). A catalyst derived from CuBTC-MeIM(rt) was also fabricated for CO oxidation, and N-CuO^T/Cu also exhibited high performance. All these results confirm that the solvent-induced coordination modulation method is a promising alternative for fabricating high-performance MOF-derived catalysts.

H_2-TPR was employed to examine the oxidation−reduction performance of three catalysts. As can be seen from Figure 8a, all catalysts showed a reduction peak before 300 °C, which was attributed to the reduction of Cu species. Among them, N-CuO/Cu presented a strong reduction peak at 206 °C, and N-CuO(ex) and N-CuO(op) showed reduction peaks at 223 and 296 °C, respectively, indicating that N-CuO/Cu has the best redox characteristics. Combined with the previous dispersion test results, the reduction temperature of CuO species had a certain correlation with the dispersion. The higher the dispersion, the lower the reduction peak temperature of CuO was. This is because higher dispersed CuO species strengthened the interaction between the carrier and the active component, thereby reducing the reduction temperature of CuO. In situ DRIFTS was performed to study the active sites and identify the reaction pathway. Taking the N-CuO/Cu catalyst with the best catalytic performance as an example, Figure 8b shows the CO/O_2 co-adsorption on the N-CuO/Cu sample at 100 °C for 20 min after the infrared spectrum. During the CO flow, the in situ DRIFTS showed two peaks at 2106 and 2174 cm^{-1}, corresponding to the vibration and adsorption peaks of gas-phase CO.[57] In addition, the infrared vibration peaks at the wavenumbers of 2342 and 2359 cm^{-1} were attributed to gas-phase CO_2. Obviously, CO and O_2 react on the surface to form CO_2 under heating operation conditions of 100 °C.

Stability is an important indicator for examining the behavior of catalysts. In the experiment, the hydrothermal stability and cycle stability of the prepared catalysts were tested. Under dry feed gas conditions, the as-prepared N-doped CuO/Cu maintained approximately 85% CO conversion at 130 °C for more than 72 h (Figure S7). The repeatability of the catalyst was tested, and the catalytic effect was almost unchanged after four cycles (Figure S8), displaying excellent stability in catalysis. Although transition metal oxides can replace traditional noble metals for catalytic reactions, H_2O dissociative adsorption usually occurs on the surface of metal oxides and the adsorbed H_2O interacts with CO to form carbonates, resulting in the poisoning and inactivation of surface active sites, which greatly limits their practical application for low-temperature CO oxidation.[12,13] In this work, about 2% water vapor was used to test the water resistance of heteroatom-doped transition metal oxides derived from dual-ligand MOFs. As illustrated in Figure 7f, even though the presence of H_2O in the feed gas reduced the conversion rate of CO, N-CuO/Cu still achieved a total conversion at 170 °C under humid conditions. By making use of basic copper nitrate as the metal node, Cu(111) produced after pyrolysis showed low oxidation activity on the surface. This inert surface reduced the dissociative adsorption of H_2O and improved the water resistance of CuO.[58] On the other hand, N doping reduced the formation of surface OH, thereby mitigating water poisoning on the surface of N-CuO/Cu.[58] As mentioned above, N-CuO/Cu catalysts reached a total CO conversion at 140 °C under dry conditions, and the difference between the reaction temperature of complete oxidation in dry and moist environments (ΔT) was as small as 30 °C. Comparatively, in previously reported studies, the ΔT of most transition metal oxides were higher than 100 °C (Table S3). As expected, the unique structure and properties of CuO/Cu and the heteroatom doping can effectively overcome the problem that the transition metal oxides are easily poisoned under moist conditions.

3. CONCLUDING REMARKS

In this study, based on the high density of heterogeneous nucleation sites of insoluble metal complex, we have achieved the transformation of dual-ligand MOFs into hierarchical N-doped metal-based composites by solvent-induced coordination modulation combined with low-temperature pyrolysis. The combination of MOF sol self-assembly with simultaneous ligand exchange can not only effectively avoid the problem of dual ligand competition in one-pot synthesis but also prevent the structural collapse caused by ligand exchange, which realized the self-assembly of dual-ligand MOFs with good crystallinity. After pyrolysis, a fusiform insoluble copper complex produced a unique Cu(111)/C matrix with enhanced oxygen binding capacity, and the strong directional binding energy with double ligands promotes the hierarchical

https://doi.org/10.1021/acsomega.1c03877
ACS Omega 2021, 6, 29596−29608

generation of CuO. The optimized N-CuO/Cu catalyst afforded remarkable catalytic performance (100% CO conversion at 140 °C) for more than 72 h with the lowest apparent activation energy (36 kJ mol^{-1}). Importantly, since N doping generated more surface active oxygen sites and reduced the formation of surface OH, the prepared N-CuO/Cu exhibited attractive water-resisting property (total conversion at 170 °C) and superior catalytic activity (TOF of 1.17×10^{-3} s^{-1} at 120 °C) for CO oxidation. This strategy can be extended to produce other metal-based multi-ligand MOFs and may open a new venue in preparing high-performance multi-heteroatom-doped materials for versatile applications.

4. THEORETICAL CONSIDERATIONS

The formula of turnover frequencies for all samples can be calculated as follows:

$$\mathrm{TOF} = \frac{PV}{RT} \times \mathrm{CO\ vol\%} \times \mathrm{conversion\%} \times \frac{M_{\mathrm{Cu}}}{m \times D_{\mathrm{Cu}}} \times \frac{1}{t} \quad (1)$$

where P is the pressure (Pa), V/t is the volume of reactant gases through the reactor every second (m^3/s), R is the gas constant, T is the room temperature (K), m is the mass of Cu species (g), M is the relative atomic mass (g/mol), and D_{Cu} is the dispersion of Cu on catalysts.

The specific reaction rate K can be calculated assuming the ideal gas behavior as follows:

$$K\ (\mathrm{mol\ g^{-1}\ s^{-1}}) = \mathrm{GHSV}\ (\mathrm{mL\ h^{-1}\ g^{-1}}) \times 1/3600\ (\mathrm{h\ s^{-1}}) \times 1/1000\ (\mathrm{L\ mL^{-1}}) \times \mathrm{CO\ vol\%} \times \mathrm{conversion\%} \times 1/22.4\ (\mathrm{mol\ L^{-1}}) \quad (2)$$

Calculation of activation energy according to the Arrhenius equation:

$$K = A\exp(-E_a/RT) \quad (3)$$

where K is the reaction rate of CO (mol CO g^{-1} s^{-1}), A is the pre-exponential factor (s^{-1}), E_a is the apparent activation energy (kJ mol^{-1}), R is the gas constant, and T is the absolute temperature (K). Taking the natural log of both sides of eq 2, we get

$$\ln K = -E_a/T + \ln A \quad (4)$$

By plotting ln K versus $1000/T$, the apparent activation energy E_a can be calculated from the slope as shown in the figure.

5. EXPERIMENTAL SECTION

5.1. Materials. All reagents were purchased commercially and used without further purification. $Cu(NO_3)_2{\cdot}3H_2O$ (99%) in A.R. grade was purchased from Sinopharm Chemical Reagent Co., Ltd., China. 2-Methylimidazole (2-MeIM, 98%), terephthalic acid (H_2BDC, 99%), and trimesic acid (H_3BTC, 98%) were purchased from Aladdin Industrial Co. *N*,*N*-Dimethylformamide (DMF) and methanol (MeOH) in A.R. grade were purchased from Lingfeng Chemical Reagent Co., Ltd., China.

5.2. Synthesis of $Cu_2(OH)_3(NO_3)$. $Cu(NO_3)_2{\cdot}3H_2O$ (2 mmol) was dissolved into DMF; after ultrasonic dissolution, the solution was allowed to stand at room temperature, and the color of the solution changes from blue to green, indicating the formation of basic copper nitrate solution.

5.3. Synthesis of CuBDC Sol. H_2BDC solution (2 mmol of H_2BDC in DMF) was added into basic copper nitrate solution and mixed well. The blue sol was centrifuged, washed several times with MeOH, and dried.

5.4. Synthesis of CuBDC by a Conventional Method. CuBDC was synthesized by a conventional solution method. The solutions of $Cu(NO_3)_2{\cdot}3H_2O$ (2 mmol) in DMF and H_2BDC (2 mmol) in DMF were mixed and placed in a water bath at 323 K. After cooling, the resulting blue powders were isolated under centrifugation, washed with MeOH several times, and dried.

5.5. Synthesis of CuBDC-MeIM(rt). 2-MeIM solution (10 mmol 2-MeIM in MeOH) was added into the above CuBDC sol solution. The color of the solution quickly changed from blue to purple. The purple solution was washed several times with MeOH and dried to obtain a purple powder.

5.6. Synthesis of CuBDC(MeIM). $Cu(NO_3)_2{\cdot}3H_2O$ (2 mmol) and H_2BDC (2 mmol) were dissolved in MeOH and DMF, respectively, and 2-MeIM were dissolved in MeOH. After the three solutions were ultrasonically homogenized, the solutions of Cu^{2+}/MeOH and H_2BDC/DMF were mixed, then mixed with 2-MeIM solution, and stirred. Finally, the resulting blue powders were isolated under centrifugation, washed with MeOH several times, and dried.

5.7. Synthesis of CuBDC-MeIM(ex) by a Post-synthetic Exchange Strategy. A certain amount of prepared CuBDC was weighed, dissolved in DMF solution, and added with a methanol solution of 2-MeIM. After ultrasonication, the mixture was transferred to a Teflon-lined autoclave and reacted at 120 °C for 24−48 h. The final product was washed several times with MeOH and dried at 80 °C.

5.8. Synthesis of CuBDC-MeIM(op) by a One-Pot Method. $Cu(NO_3)_2{\cdot}3H_2O$ (2 mmol), H_2BDC (2 mmol), and 2-MeIM (10 mmol) were dissolved in MeOH, DMF, and MeOH, respectively. The three solutions were mixed and then transferred to a Teflon-lined autoclave at 120 °C for 24−48 h. The final product was washed several times with MeOH and dried at 80 °C.

5.9. Fabrication of N-Doped CuO/Cu. CuBDC-MeIM-(rt) was heated to 300 °C at a rate of 5 °C/min under an air atmosphere. Other derivatives were obtained through the same pyrolysis procedure.

5.10. Characterization. The surface morphology of the prepared samples was evaluated by scanning electron microscopy (SEM, TM-1000, Hitachi, Japan) and transmission electron microscopy (TEM, JEM-1200EX, Hitachi, Japan). The change of the chemical structure was analyzed by FTIR spectroscopy (Nicolet 6700, Thermo Scientific Co., USA). Powder X-ray diffraction (XRD) data were recorded on a PANalytical X'Pert PRO X-ray diffractometer using Cu Kα X-rays. Energy-dispersive spectroscopy (EDS, S-3700 N, Hitachi, Japan) was taken for the composition detection of different samples. The specific surface areas and pore size distribution of the samples were determined using Brunauer−Emmett−Teller (BET) and Barrett−Joyner−Halenda (BJH) analysis at a Micromeritics instrument (ASAP 2020). The X-ray photoelectron spectroscopy (XPS) experiments were carried out on an RBD upgraded PHI-5000C ESCA system (Perkin Elmer) with Mg K radiation (h = 1253.6 eV), and binding energies were calibrated by using the containment carbon (C 1s = 284.5 eV). The compositional analysis of catalysts was performed by

https://doi.org/10.1021/acsomega.1c03877
ACS Omega 2021, 6, 29596−29608

ICP-AES in an Optima 2000 instrument (PerkinElmer, USA). TG measurements were carried out by a thermal gravimetric analyzer (PERKIN ELMER, Model TGA 7). H_2 temperature-programmed reduction (H_2-TPR) experiments were carried out in an AutoChem II 2920 V3.05 equipped with a thermal conductivity detector by using the 10% H_2/Ar gas flow.

The dispersion of surface copper atoms was estimated via N_2O oxidation and followed by H_2 titration according to the literature.[59] In brief, the sample was first pretreated at 300 °C for 1 h in Ar flow and cooled to 50 °C. Second, it was exposed to a reduction gas (5% H_2/N_2 mixture, 30 mL/min) and the reactor was heated to 300 °C in 10 °C/min, and the amount of hydrogen consumption in the first TPR was denoted as X. Third, the catalyst was cooled down to 50 °C, and the surface Cu atoms were oxidized to Cu_2O by N_2O (30 mL/min) at 50 °C for 1 h. The reactor was purged with Ar for 2 h in order to remove the excess N_2O. Finally, another TPR experiment was performed in 5% H_2/N_2 at a flow rate of 30 mL/min, and the amount of hydrogen consumption in later TPR was denoted as Y. The dispersion of surface Cu (D) and the area of surface Cu (S) were calculated according to the following equations:

Reduction of all Cu atoms:

$$CuO + H_2 \rightarrow Cu + H_2O, \text{ hydrogen consumption} = X$$

Reduction of surface Cu atoms only:

$$Cu_2O + H_2 \rightarrow 2Cu + H_2O, \text{ hydrogen consumption} = Y$$

The dispersion of surface Cu was calculated as

$$D = 2 \times Y/X \times 100\% \quad (5)$$

The area of surface Cu was calculated as

$$S = 2 \times Y \times \frac{N_{av}}{X \times M_{Cu} \times 1.4 \times 10^{19}} = 1353 \times \frac{Y}{X}\ (m^2 - Cu/g - Cu) \quad (6)$$

In these equations, N_{av} is Avogadro's constant, M_{Cu} is the relative atomic mass of copper (63.46 g/mol), and 1.4×10^{19} is the number of copper atoms of per square meter.

In situ DRIFTS was performed on a Nicolet iS-50 spectrometer equipped with an MCT detector cooled by liquid nitrogen. Before measurement, the sample powder (30 mg) was purged by a N_2 stream at 200 °C with a flow rate of 30 mL min^{-1} to eliminate impurities and the physically absorbed water. After cooling to room temperature, a background spectrum was collected for spectral correction. Then, 1% CO, 1% O_2, and balanced N_2 at a total flow rate of 30 mL min^{-1} were introduced into the in situ chamber, and the spectra were recorded at 100 °C.

5.11. Catalytic Experiments. In the experiment, the catalytic oxidation performance of the catalysts was measured on a self-made atmospheric fixed bed microreactor. Then, 100 mg of MOF-based catalyst was placed in a Φ8 × 1 mm quartz reactor, and a mixed gas (1 vol % CO, 1 vol % O_2, and 98 vol % N_2) was introduced at a flow rate of 60 mL/min. The temperature is programmed by a tubular resistance furnace, and the outlet tail gas flow is connected to a gas chromatograph (GC 1690) for online analysis via a six-way sampling valve.

■ ASSOCIATED CONTENT

Supporting Information

The Supporting Information is available free of charge at https://pubs.acs.org/doi/10.1021/acsomega.1c03877.

Tyndall light scattering effect, SEM image and TEM image of CuBDC, XPS spectra, long-term durability test of as-prepared catalysts, reusability of catalysts after subsequent reactions, textural properties of 300 °C-calcined CuO samples, comparison of preparation methods of different MOF precursors and comparison of CO catalytic effects of MOF-based catalysts, and comparison of CO complete conversion under normal and moisture-rich conditions with references (PDF)

■ AUTHOR INFORMATION

Corresponding Author

Guoliang Zhang − *Institute of Oceanic and Environmental Chemical Engineering, Center for Membrane and Water Science & Technology, State Key Lab Breeding Base of Green Chemical Synthesis Technology, Zhejiang University of Technology, Hangzhou 310014, P.R. China;* orcid.org/0000-0002-7371-3349; Phone: 86-571-88320863; Email: guoliangz@zjut.edu.cn

Authors

Jingwen Mao − *Institute of Oceanic and Environmental Chemical Engineering, Center for Membrane and Water Science & Technology, State Key Lab Breeding Base of Green Chemical Synthesis Technology, Zhejiang University of Technology, Hangzhou 310014, P.R. China*

Lei Qin − *Institute of Oceanic and Environmental Chemical Engineering, Center for Membrane and Water Science & Technology, State Key Lab Breeding Base of Green Chemical Synthesis Technology, Zhejiang University of Technology, Hangzhou 310014, P.R. China*

Lin Tian − *Institute of Oceanic and Environmental Chemical Engineering, Center for Membrane and Water Science & Technology, State Key Lab Breeding Base of Green Chemical Synthesis Technology, Zhejiang University of Technology, Hangzhou 310014, P.R. China*

Lantian He − *Institute of Oceanic and Environmental Chemical Engineering, Center for Membrane and Water Science & Technology, State Key Lab Breeding Base of Green Chemical Synthesis Technology, Zhejiang University of Technology, Hangzhou 310014, P.R. China*

Yujie Zhu − *Institute of Oceanic and Environmental Chemical Engineering, Center for Membrane and Water Science & Technology, State Key Lab Breeding Base of Green Chemical Synthesis Technology, Zhejiang University of Technology, Hangzhou 310014, P.R. China*

Qin Meng − *College of Chemical and Biochemical Engineering, State Key Laboratory of Chemical Engineering, Zhejiang University, Hangzhou 310027, P.R. China;* orcid.org/0000-0002-8017-6852

Complete contact information is available at: https://pubs.acs.org/10.1021/acsomega.1c03877

Notes

The authors declare no competing financial interest.

https://doi.org/10.1021/acsomega.1c03877
ACS Omega 2021, 6, 29596−29608

■ ACKNOWLEDGMENTS

This work was supported by the National Natural Science Foundation of China (nos. 21736009 and 21808202), the Zhejiang Provincial Bureau of Science and Technology, China (grants no. 2021C03169), SINOPEC Science and Technology Development Project from China Petrochemical Corporation (no. 33750000-20-ZC0607-0012), and Tongjiang Scholarship from Fujian Quanzhou Government.

■ ABBREVIATIONS

CuBDC	prepared by a conventional solution method
CuBDC(MeIM)	prepared by a coordination modulation method
CuBDC-MeIM(rt)	prepared by a solvent-induced coordination modulation method at room temperature
CuBDC-MeIM(ex)	prepared by post-synthesis exchange method
CuBDC-MeIM(op)	prepared by the one-pot method
CuO	derived from CuBDC
CuO(sol)	derived from CuBDC sol
N-CuO/Cu	derived from CuBDC-MeIM(rt)
N-CuO(ex)	derived from CuBDC-MeIM(ex)
N-CuO(op)	derived from CuBDC-MeIM(op)
CuBTC	prepared by a conventional solution method
CuBTC-MeIM(rt)	prepared by a solvent-induced coordination modulation method at room temperature
CuO^T	derived from CuBTC
CuO^T(sol)	derived from the CuBTC sol
N-CuO^T/Cu	derived from CuBTC-MeIM(rt)

■ REFERENCES

(1) Al Soubaihi, R.; Saoud, K.; Dutta, J. Critical Review of Low-Temperature CO Oxidation and Hysteresis Phenomenon on Heterogeneous Catalysts. *Catalysts* **2018**, *8*, 660.

(2) Rodriguez, J. A.; Grinter, D. C.; Liu, Z.; Palomino, R. M.; Senanayake, S. D. Ceria-based model catalysts: fundamental studies on the importance of the metal-ceria interface in CO oxidation, the water-gas shift, CO_2 hydrogenation, and methane and alcohol reforming. *Chem. Soc. Rev.* **2017**, *46*, 1824−1841.

(3) Xu, Z.; Zhang, Y.; Qin, L.; Meng, Q.; Xue, Z.; Qiu, L.; Zhang, G.; Guo, X.; Li, Q. Crystal Facet Induced Single-Atom Pd/Co_xO_y on a Tunable Metal-Support Interface for Low Temperature Catalytic Oxidation. *Small* **2020**, *16*, No. e2002071.

(4) Shi, L.-Y.; Li, Y.-X.; Xue, D.-M.; Shao, M.-Q.; Gu, M.-X.; Liu, X.-Q.; Sun, L.-B. Facile Fabrication of Small-Sized Palladium Nanoparticles in Nanoconfined Spaces for Low-Temperature CO Oxidation. *Ind. Eng. Chem. Res.* **2020**, *59*, 19145−19152.

(5) Ishida, T.; Murayama, T.; Taketoshi, A.; Haruta, M. Importance of Size and Contact Structure of Gold Nanoparticles for the Genesis of Unique Catalytic Processes. *Chem. Rev.* **2020**, *120*, 464−525.

(6) Doherty, F.; Wang, H.; Yang, M.; Goldsmith, B. R. Nanocluster and single-atom catalysts for thermocatalytic conversion of CO and CO_2. *Catal. Sci. Technol.* **2020**, *10*, 5772−5791.

(7) Wang, H.; Shen, J. H.; Huang, J. F.; Xu, T. J.; Zhu, J. R.; Zhu, Y. H.; Li, C. Z. Atomically dispersed Au catalysts supported on CeO_2 foam: controllable synthesis and CO oxidation reaction mechanism. *Nanoscale* **2017**, *9*, 16817−16825.

(8) He, J.; Chen, D.; Li, N.; Xu, Q.; Li, H.; He, J.; Lu, J. Hollow Mesoporous Co_3O_4-CeO_2 Composite Nanotubes with Open Ends for Efficient Catalytic CO Oxidation. *ChemSusChem* **2019**, *12*, 1084−1090.

(9) Papavasiliou, J.; Rawski, M.; Vakros, J.; Avgouropoulos, G. A Novel Post-Synthesis Modification of CuO-CeO_2 Catalysts: Effect on Their Activity for Selective CO Oxidation. *ChemCatChem* **2018**, *10*, 2096−2106.

(10) Liu, G.; Yu, J.; Chen, L.; Feng, N.; Meng, J.; Fang, F.; Zhao, P.; Wang, L.; Wan, H.; Guan, G. Promoting Diesel Soot Combustion Efficiency over Hierarchical Brushlike α-MnO_2 and Co_3O_4 Nanoarrays by Improving Reaction Sites. *Ind. Eng. Chem. Res.* **2019**, *58*, 13935−13949.

(11) Voskanyan, A. A.; Tsui, J. C.-K.; Chan, K.-Y. Durable ruthenium oxide/ceria catalyst with ultralarge mesopores for low-temperature CO oxidation. *J. Catal.* **2020**, *382*, 155−164.

(12) D'Agostino, C.; Chansai, S.; Bush, I.; Gao, C.; Mantle, M. D.; Hardacre, C.; James, S. L.; Gladden, L. F. Assessing the effect of reducing agents on the selective catalytic reduction of NOx over Ag/Al_2O_3 catalysts. *Catal. Sci. Technol.* **2016**, *6*, 1661−1666.

(13) Kuo, C.-H.; Li, W.; Song, W.; Luo, Z.; Poyraz, A. S.; Guo, Y.; Ma, A. W. K.; Suib, S. L.; He, J. Facile Synthesis of Co_3O_4@CNT with High Catalytic Activity for CO Oxidation under Moisture-Rich Conditions. *ACS Appl. Mater. Interfaces* **2014**, *6*, 11311−11317.

(14) Liu, Y.; Mao, D.; Yu, J.; Zheng, Y.; Guo, X. Facile preparation of highly active and stable CuO-CeO_2 catalysts for low-temperature CO oxidation via a direct solvothermal method. *Catal. Sci. Technol.* **2020**, *10*, 8383−8395.

(15) Wang, B.; Zhang, H.; Xu, W.; Li, X.; Wang, W.; Zhang, L.; Li, Y.; Peng, Z.; Yang, F.; Liu, Z. Nature of Active Sites on Cu−CeO_2 Catalysts Activated by High Temperature Thermal Aging. *ACS Catal.* **2020**, *10*, 12385−12392.

(16) Nie, L.; Mei, D.; Xiong, H.; Peng, B.; Ren, Z.; Hernandez, X. I. P.; DeLariva, A.; Wang, M.; Engelhard, M. H.; Kovarik, L.; Datye, A. K.; Wang, Y. Activation of surface lattice oxygen in single-atom Pt-CeO_2 for low-temperature CO oxidation. *Science* **2017**, *358*, 1419−1423.

(17) Howarth, A. J.; Liu, Y.; Li, P.; Li, Z.; Wang, T. C.; Hupp, J. T.; Farha, O. K. Chemical, thermal and mechanical stabilities of metal−organic frameworks. *Nat. Rev. Mater.* **2016**, *1*, 15018.

(18) Li, W.; Zhang, Y.; Zhang, C.; Meng, Q.; Xu, Z.; Su, P.; Li, Q.; Shen, C.; Fan, Z.; Qin, L.; Zhang, G. Transformation of metal-organic frameworks for molecular sieving membranes. *Nat. Commun.* **2016**, *7*, 11315.

(19) Dang, S.; Zhu, Q.-L.; Xu, Q. Nanomaterials derived from metal−organic frameworks. *Nat. Rev. Mater.* **2017**, *3*, 17075.

(20) Qin, L.; Ru, R.; Mao, J.; Meng, Q.; Fan, Z.; Li, X.; Zhang, G. Assembly of MOFs/polymer hydrogel derived Fe_3O_4-CuO@hollow carbon spheres for photochemical oxidation: Freezing replacement for structural adjustment. *Appl. Catal., B* **2020**, *269*, 118754.

(21) Zhang, S.; Li, H.; Liu, P.; Ma, L.; Li, L.; Zhang, W.; Meng, F.; Li, L.; Yang, Z.; Wu, T.; Huo, F.; Lu, J. Directed Self-Assembly of MOF-Derived Nanoparticles toward Hierarchical Structures for Enhanced Catalytic Activity in CO Oxidation. *Adv. Energy Mater.* **2019**, *9*, 1901754.

(22) Yang, Y.; Dong, H.; Wang, Y.; He, C.; Wang, Y.; Zhang, X. Synthesis of octahedral like Cu-BTC derivatives derived from MOF calcined under different atmosphere for application in CO oxidation. *J. Solid State Chem.* **2018**, *258*, 582−587.

(23) Zhang, X.; Hou, F.; Yang, Y.; Wang, Y.; Liu, N.; Chen, D.; Yang, Y. A facile synthesis for cauliflower like CeO_2 catalysts from Ce-BTC precursor and their catalytic performance for CO oxidation. *Appl. Surf. Sci.* **2017**, *423*, 771−779.

(24) Abney, C. W.; Patterson, J. T.; Gilhula, J. C.; Wang, L.; Hensley, D. K.; Chen, J.; Foo, G. S.; Wu, Z.; Dai, S. Controlling interfacial properties in supported metal oxide catalysts through metal-organic framework templating. *J. Mater. Chem. A* **2017**, *5*, 13565−13572.

(25) Shao, Y.; Zhang, J.; Jiang, H.; Chen, R. Well-Defined MOF-Derived Hierarchically Porous N-Doped Carbon Materials for the Selective Hydrogenation of Phenol to Cyclohexanone. *Ind. Eng. Chem. Res.* **2021**, *60*, 5806−5815.

https://doi.org/10.1021/acsomega.1c03877
ACS Omega 2021, 6, 29596−29608

(26) Xu, Z.; Huang, C.; Wang, L.; Pan, X.; Qin, L.; Guo, X.; Zhang, G. Sulfate Functionalized Fe_2O_3 Nanoparticles on TiO_2 Nanotube as Efficient Visible Light-Active Photo-Fenton Catalyst. *Ind. Eng. Chem. Res.* **2015**, *54*, 4593−4602.
(27) Qin, L.; Xu, Z.; Zheng, Y.; Li, C.; Mao, J.; Zhang, G. Confined Transformation of Organometal-Encapsulated MOFs into Spinel $CoFe_2O_4$/C Nanocubes for Low-Temperature Catalytic Oxidation. *Adv. Funct. Mater.* **2020**, *30*, 1910257.
(28) Chen, B.; Yang, X.; Zeng, X.; Huang, Z.; Xiao, J.; Wang, J.; Zhan, G. Multicomponent metal oxides derived from Mn-BTC anchoring with metal acetylacetonate complexes as excellent catalysts for VOCs and CO oxidation. *Chem. Eng. J.* **2020**, *397*, 125424.
(29) Zhang, Q. Q.; Liu, X. F.; Ma, L.; Wei, Y. S.; Wang, Z. Y.; Xu, H.; Zang, S. Q. Remoulding a MOF's pores by auxiliary ligand introduction for stability improvement and highly selective CO_2-capture. *Chem. Commun.* **2018**, *54*, 12029−12032.
(30) Sumida, K.; Moitra, N.; Reboul, J.; Fukumoto, S.; Nakanishi, K.; Kanamori, K.; Furukawa, S.; Kitagawa, S. Mesoscopic superstructures of flexible porous coordination polymers synthesized via coordination replication. *Chem. Sci.* **2015**, *6*, 5938−5946.
(31) Li, A.; Song, H.; Bian, Z.; Shi, L.; Chen, X.; Zhou, J. ZnO nanosheet/squeezebox-like porous carbon composites synthesized by in situ pyrolysis of a mixed-ligand metal-organic framework. *J. Mater. Chem. A* **2017**, *5*, 5934−5942.
(32) Qin, L.; Li, Z.; Hu, Q.; Xu, Z.; Guo, X.; Zhang, G. One-pot assembly of metal/organic-acid sites on amine-functionalized ligands of MOFs for photocatalytic hydrogen peroxide splitting. *Chem. Commun.* **2016**, *52*, 7110−7113.
(33) Kim, H.; Kim, D.; Moon, D.; Choi, Y. N.; Baek, S. B.; Lah, M. S. Symmetry-guided syntheses of mixed-linker Zr metal-organic frameworks with precise linker locations. *Chem. Sci.* **2019**, *10*, 5801−5806.
(34) Karagiaridi, O.; Bury, W.; Mondloch, J. E.; Hupp, J. T.; Farha, O. K. Solvent-assisted linker exchange: an alternative to the de novo synthesis of unattainable metal-organic frameworks. *Angew. Chem., Int. Ed.* **2014**, *53*, 4530−4540.
(35) Cao, L. H.; Xu, X. Q.; Tang, X. H.; Yang, Y.; Liu, J.; Yin, Z.; Zang, S. Q.; Ma, Y. M. Controllable Strategy for Metal-Organic Framework Light-Driven [2 + 2] Cycloaddition Reactions via Solvent-Assisted Linker Exchange. *Inorg. Chem.* **2021**, *60*, 2117−2121.
(36) Joshi, J. N.; Moran, C. M.; Feininger, H. P.; Dow, J. M.; Walton, K. S. Household Aluminum Products as Insoluble Precursors for Directed Growth of Metal−Organic Frameworks. *Cryst. Growth Des.* **2019**, *19*, 5097−5104.
(37) Wang, Z.; Ge, L.; Li, M.; Lin, R.; Wang, H.; Zhu, Z. Orientated growth of copper-based MOF for acetylene storage. *Chem. Eng. J.* **2019**, *357*, 320−327.
(38) Liu, X. L.; Fan, W. W.; Lu, Z. X.; Qin, Y.; Yang, S. X.; Li, Y.; Liu, Y. X.; Zheng, L. Y.; Cao, Q. E. Solvent-Driven Reversible Phase Transition of a Pillared Metal-Organic Framework. *Chem. − Eur. J.* **2019**, *25*, 5787−5792.
(39) Singh, N.; Ahmed, S.; Fakim, A.; Qutub, S.; Alahmed, O.; El Tall, O.; Shekhah, O.; Eddaoudi, M.; Khashab, N. M. In situ assembled ZIF superstructures via an emulsion-free soft-templating approach. *Chem. Sci.* **2020**, *11*, 11280−11284.
(40) Chaudhari, A. K.; Han, I.; Tan, J. C. Multifunctional Supramolecular Hybrid Materials Constructed from Hierarchical Self-Ordering of In Situ Generated Metal-Organic Framework (MOF) Nanoparticles. *Adv. Mater.* **2015**, *27*, 4438−4446.
(41) Toyao, T.; Liang, K.; Okada, K.; Ricco, R.; Styles, M. J.; Tokudome, Y.; Horiuchi, Y.; Hill, A. J.; Takahashi, M.; Matsuoka, M.; Falcaro, P. Positioning of the HKUST-1 metal-organic framework ($Cu_3(BTC)_2$) through conversion from insoluble Cu-based precursors. *Inorg. Chem. Front.* **2015**, *2*, 434−441.
(42) Hou, J. W.; Sapnik, A. F.; Bennett, T. D. Metal-organic framework gels and monoliths. *Chem. Sci.* **2020**, *11*, 310−323.
(43) Ullah, S.; Akram, B.; Ali, H.; Zhang, H.; Yang, H.; Liu, Q.; Wang, X. 2-Methylimidazole assisted ultrafast synthesis of carboxylate-based metal−organic framework nano-structures in aqueous medium at room temperature. *Sci. Bull.* **2019**, *64*, 1103−1109.
(44) Guo, C.; Zhang, Y. H.; Zhang, L.; Zhang, Y.; Wang, J. 2-Methylimidazole-assisted synthesis of a two-dimensional MOF-5 catalyst with enhanced catalytic activity for the Knoevenagel condensation reaction. *CrystEngComm* **2018**, *20*, 5327−5331.
(45) Guo, C.; Zhang, Y.; Guo, Y.; Zhang, L.; Zhang, Y.; Wang, J. A general and efficient approach for tuning the crystal morphology of classical MOFs. *Chem. Commun.* **2018**, *54*, 252−255.
(46) Li, X.; Zhou, H.; Qi, F.; Niu, X.; Xu, X.; Qiu, F.; He, Y.; Pan, J.; Ni, L. Three hidden talents in one framework: a terephthalic acid-coordinated cupric metal-organic framework with cascade cysteine oxidase- and peroxidase-mimicking activities and stimulus-responsive fluorescence for cysteine sensing. *J. Mater. Chem. B* **2018**, *6*, 6207−6211.
(47) Yang, Q.; Ren, S.; Zhao, Q.; Lu, R.; Hang, C.; Chen, Z.; Zheng, H. Selective separation of methyl orange from water using magnetic ZIF-67 composites. *Chem. Eng. J.* **2018**, *333*, 49−57.
(48) Wang, F.; Chen, X.; Chen, L.; Yang, J.; Wang, Q. High-performance non-enzymatic glucose sensor by hierarchical flower-like nickel(II)-based MOF/carbon nanotubes composite. *Mater. Sci. Eng., C* **2019**, *96*, 41−50.
(49) Mondal, I.; Gonuguntla, S.; Pal, U. Photoinduced Fabrication of Cu/TiO_2 Core−Shell Heterostructures Derived from Cu-MOF for Solar Hydrogen Generation: The Size of the Cu Nanoparticle Matters. *J. Phys. Chem. C* **2019**, *123*, 26073−26081.
(50) Li, G.; Zhang, X.; Zhang, H.; Liao, C.; Jiang, G. Bottom-up MOF-intermediated synthesis of 3D hierarchical flower-like cobalt-based homobimetallic phophide composed of ultrathin nanosheets for highly efficient oxygen evolution reaction. *Appl. Catal., B* **2019**, *249*, 147−154.
(51) Tang, J.; Shen, Y.; Miao, X.; Qin, H.; Song, D.; Li, Y.; Qu, Y.; Yin, Z.; Ren, J.; Wang, L.; Wang, B. Template-directed growth of hierarchically structured MOF-derived LDH cage hybrid arrays for supercapacitor electrode. *J. Electroanal. Chem.* **2019**, *840*, 174−181.
(52) Kropp, T.; Mavrikakis, M. Transition Metal Atoms Embedded in Graphene: How Nitrogen Doping Increases CO Oxidation Activity. *ACS Catal.* **2019**, *9*, 6864−6868.
(53) Gao, Y.; Zhang, L.; van Hoof, A. J. F.; Hensen, E. J. M. On the surface-dependent oxidation of Cu_2O during CO oxidation: Cu^{2+} is more active than Cu^{+}. *Appl. Catal., A* **2020**, *602*, 117712.
(54) Xu, X.; Li, L.; Huang, J.; Jin, H.; Fang, X.; Liu, W.; Zhang, N.; Wang, H.; Wang, X. Engineering Ni^{3+} Cations in NiO Lattice at the Atomic Level by Li^{+} Doping: The Roles of Ni^{3+} and Oxygen Species for CO Oxidation. *ACS Catal.* **2018**, *8*, 8033−8045.
(55) Zhang, Z.; Liu, T.; Fu, B.; Yang, X.; Zhang, D. H. First-principles quantum dynamical theory for the dissociative chemisorption of H_2O on rigid Cu(111). *Nat. Commun.* **2016**, *7*, 11953.
(56) Yang, F.; Graciani, J.; Evans, J.; Liu, P.; Hrbek, J.; Sanz, J. F.; Rodriguez, J. A. CO oxidation on inverse CeOx/Cu(111) catalysts: high catalytic activity and ceria-promoted dissociation of O_2. *J. Am. Chem. Soc.* **2011**, *133*, 3444−3451.
(57) Wang, W.-W.; Du, P.-P.; Zou, S.-H.; He, H.-Y.; Wang, R.-X.; Jin, Z.; Shi, S.; Huang, Y.-Y.; Si, R.; Song, Q.-S.; Jia, C.-J.; Yan, C.-H. Highly Dispersed Copper Oxide Clusters as Active Species in Copper-Ceria Catalyst for Preferential Oxidation of Carbon Monoxide. *ACS Catal.* **2015**, *5*, 2088−2099.
(58) Bae, J.; Shin, D.; Jeong, H.; Kim, B.-S.; Han, J. W.; Lee, H. Highly Water-Resistant La-Doped Co_3O_4 Catalyst for CO Oxidation. *ACS Catal.* **2019**, *9*, 10093−10100.
(59) Xia, S.; Nie, R.; Lu, X.; Wang, L.; Chen, P.; Hou, Z. Hydrogenolysis of glycerol over $Cu_{0.4}/Zn_{5.6-x}Mg_xAl_2O_{8.6}$ catalysts: The role of basicity and hydrogen spillover. *J. Catal.* **2012**, *296*, 1−11.

https://doi.org/10.1021/acsomega.1c03877
ACS Omega 2021, 6, 29596−29608